Dynamics of Atmospheres and Oceans 90 (2020) 101141

Contents lists available at ScienceDirect

Dynamics of Atmospheres and Oceans

journal homepage: www.elsevier.com/locate/dynatmoce

The influence of the Madden-Julian oscillation on high-latitude surface air temperature during boreal winter

Jing Cui[a], Shuangyan Yang[a,*], Tim Li[a,b]

[a] Key Laboratory of Meteorological Disaster, Ministry of Education (KLME)/Joint International Research Laboratory of Climate and Environmental Change (ILCEC)/Collaborative Innovation Center on Forecast and Evaluation of Meteorological Disasters (CIC-FEMD), Nanjing University of Information Science and Technology, Nanjing, China

[b] International Pacific Research Center and Department of Atmospheric Sciences, University of Hawaii at Manoa, Honolulu, HI, United States

ARTICLE INFO

Keywords:
The MJO
Surface air temperature
Rossby wave train
Wave activity flux

ABSTRACT

By analyzing NCEP-NCAR reanalysis daily data for 1979–2016, the modulation by Madden-Julian Oscillation (MJO) of the wintertime surface air temperature (SAT) over high latitude is examined. The real-time multivariate MJO (RMM) index, which divides the MJO into eight phases, is used. It is found that a significantly negative SAT anomaly over the northern high latitude region of (180°–60 °W, 60°–90 °N) lags the MJO convection for 1 ~ 2 weeks in phase 3, in which the enhanced convective activity exists over the Indian Ocean. While a significantly positive SAT anomaly appears over the same region following the MJO phase 7, as the tropical heating shows an opposite sign. Analysis of the anomalous circulation indicates that the observed SAT signal is probably a result of the northeastward propagating Rossby wave train triggered by MJO-related tropical forcing through Rossby wave energy dispersion. By using an anomalous atmospheric general circulation model (AGCM), the significant effect of tropical forcing on organizing the extratropical circulation anomaly is confirmed. Analysis of a temperature tendency equation further reveals that the intraseasonal SAT anomaly is primarily attributed to the advection of the mean temperature by the wind anomaly associated with the anomalous circulation of the MJO-related variability.

1. Introduction

The Madden-Julian Oscillation (MJO) is the most prominent physical mode of tropical intraseasonal variability in the atmosphere. The MJO is typically characterized as an eastward propagation around the globe tropics with a cycle on the order of 3060 days (Madden and Julian, 1971, 1972). Great efforts have been made to understand the dynamics and mechanisms of the tropical oscillation, including its initiation (Zhao et al., 2013) and propagation (Chang and Lim, 1988; Wang and Rui, 1990; Hsu and Li, 2012; Sobel and Maloney, 2013; Li, 2014). The MJO can modulate the weather and climate in the tropics directly (Madden and Julian, 1994), since it organizes tropical convection. For example, it has an impact on the formation and strength of tropical cyclones and hurricanes (Maloney and Hartmann, 2000; Hall et al., 2001), together with the timing of the Indian and Australian summer monsoons onsets (Lorenz and Hartmann, 2006; Pai et al., 2011). It also has impacts on the Indian Ocean dipole events (Rao and Yamagata, 2004), the Asian and North Pacific circulation anomalies (Higgins and Mo, 1997; Jia et al., 2011), and ENSO activities (Bergman et al., 1999; Takayabu et al., 1995). Many previous studies have demonstrated that the influence of the MJO on the circulation

* Corresponding author.
E-mail address: yangsy@nuist.edu.cn (S. Yang).

https://doi.org/10.1016/j.dynatmoce.2020.101141
Received 25 September 2019; Received in revised form 10 March 2020; Accepted 19 March 2020
Available online 20 March 2020
0377-0265/

anomalies is not only limited to the tropics but also extends into middle and high latitudes (Lau and Philips, 1986; Ting and Sardeshmukh, 1993), since the convective heating anomalies can modulate large-scale circulation anomalies and weather systems taking the form of wave trains (Ferranti et al., 1990; Kiladis and Weickmann, 1992). Thus, the MJO has a critical impact on the extratropical climate and weather at the subseasonal time scale. For example, Bond and Vecchi (2003) found that in the states of Oregon and Washington, there are close connections between the MJO and local wintertime precipitation. Lin and Brunet (2009) pointed out the important role of the MJO in Canadian wintertime surface air temperature (SAT). Yoo et al. (2012) investigated the mechanisms that lead to the boreal winter Arctic SAT change during different MJO phases. The link between the MJO and extreme events in boreal winter and summer was investigated by Matsueda and Takaya (2015) and Diao et al. (2018), respectively. Considering that the MJO has such great impacts on the tropical and extratropical variabilities, the intraseasonal oscillation over mid- and high-latitude has also been investigated, which turns out to have significant influence on both the extratropical and tropical circulation anomalies (Mao et al., 2010; Wen et al., 2011; Yang and Li, 2016a, b, 2017a, b; Yang et al., 2019). The mid-high-latitude intraseasonal oscillation can work together with the tropical variabilities, leading to more enhanced anomalous circulation (Hong and Li, 2009). It is found that the MJO is also connected with some mid- and high- oscillations such as the Arctic Oscillation (Zhou and Miller, 2003; L'Heureux and Higgins, 2008).

This work is motivated by the analysis of (Vecchi and Bond, 2004), in which the close relationship between the MJO and northern high-latitude SAT during boreal winter was examined. In this study we try to further understand the causes contributing to the SAT anomaly associated with the MJO and figure out the key process with the aid of temperature budget analysis. The resting paper is organized as follows. Section 2 describes the data and methodology employed. The possible causes leading to the MJO-related SAT anomalies over high latitude in the Northern Hemisphere are examined in Section 3. Section 4 presents the conclusions and discussions.

2. Data and methodology

2.1. Data

The data used for this study consist of the daily averaged interpolated outgoing longwave radiation (OLR) from National Oceanic and Atmospheric Administration (NOAA) and the re-analysis data generated by the National Centers for Environment Prediction-National Center for Atmospheric Research (NCEP-NCAR), both of which have a 2.5 horizontal resolution. The daily geopotential height, horizontal and vertical wind components, temperature at different pressure levels, and surface air temperature at 2 m (T-2 m), which is on the T62 Gaussian grid are used. The analysis period for the current study spans 37 winters from 1979/80–2015/16, including the months of November, December, January, February and March. Observed OLR is used as a proxy for convective activity over the tropical regions.

Eight separate phases of the MJO is defined using the Real-Time Multivariate MJO (RMM) index proposed by (Wheeler and Hendon, 2004), which is derived from the two leading principal components (PC1 and PC2) of the multivariate empirical orthogonal function (EOF) analysis for meridionally averaged equatorial OLR and zonal winds at 850 and 200 hPa. Because of the significant lead-lag relation of the two PCs (RMM1 and RMM2), the MJO life cycle can be naturally divided into eight separate stages, denoted as specific phases in the MJO phase diagram consisting of RMM1 and RMM2. The daily RMM index is available on the Australian Bureau of Meteorology website, detailed information about the RMM index can be found at http://www.bom.gov.au/climate/mjo/. Considering that the RMM is primarily a circulation index, we utilize an all-season OLR-based MJO index (OMI; Kiladis et al., 2014), which is directly related to the MJO convection, to compare the results with RMM. OMI has been found to have high correlations with various MJO-related indices and it turns out to be more predictable (Wang et al., 2019). The OMI index is available at https://www.esrl.noaa.gov/psd/mjo/mjoindex/. In this study, the gross features of the anomalous SAT signals and circulation of composite MJOs over high latitude are similar regardless of the index, although the OMI is characterized by stronger SAT signals in some of the lag days (figures omitted).

2.2. Methodology

In order to extract the MJO signals, we remove the slow annual cycle (mean and the first four annual harmonics of daily climatology of the 38 years (1979–2016) at the first step. Then a 30–60-day Lanczos band-pass filtering is applied to the so-derived anomaly fields. After the filtering, the data of November March was selected for the analysis, but neither January March 1979 nor November December 2016 is included.

Statistical significance for the composites based on MJO phases is judged using a *t*-test applied to the difference between two sample means. The formula is

$$t=\frac{|\overline{x}-\overline{y}|}{s(\frac{1}{m1}+\frac{1}{m2})^{1/2}} \tag{2.1}$$

where $s^2=[\sum_{i=1}^{m1}(x_i-\overline{x})^2+\sum_{i=1}^{m2}(y_i-\overline{y})^2]/(m_1^{'}+m_2^{'}\text{-}2)$, $\overline{x}$ and $\overline{y}$ are the sample means for a certain MJO phase and for all data, respectively. The effective degree of freedom is estimated considering the autocorrelation of daily data. Here is the number of strong MJO cases at a certain phase and is estimated as (Wilks, 2011)

$$m_2^{'}=m_2\frac{(1\text{-}\rho_1)}{(1+\rho_2)} \tag{2.2}$$

where ρ_1 is the lag-1 autocorrelation coefficient and m_2 is the sample size for.

To investigate the source of the Rossby wave train and its propagation direction, we calculated the Rossby wave source (RWS; Sardeshmukh and Hoskins, 1988) and the wave activity flux (WAF) vector (**W** vector; Takaya and Nakamura, 2001). The perturbation Rossby wave source is contributed by four terms:

$$S^{'}=-\overline{\zeta}\nabla\bullet v_x^{'}-v_x^{'}\bullet\nabla\overline{\zeta}-\zeta\bullet\nabla\overline{v}_x-\overline{v}_x\nabla\bullet\zeta^{'} \tag{2.3}$$

In Eq. (2.3), the terms with overbars denote the basic state and primes indicate MJO time scale component. Here is the absolute vorticity and denotes the divergent wind at 200 hPa. Mori and Watanabe (2008) and Seo and Lee (2017) have demonstrated that the first two terms on the right side of Eq. (2.3) are the dominant terms on MJO time scales. The two terms indicate the stretching of climatological absolute vorticity by the anomalous divergent flow ($-\overline{\zeta}\nabla\bullet v_x^{'}$) and the advection of climatological absolute vorticity by the divergent component of the anomalous wind ($-v_x^{'}\bullet\nabla\overline{\zeta}$). The perturbation Rossby wave source has been widely used in the study of the MJO teleconnection patterns (Seo and Lee, 2017; Tseng et al., 2019).

A two dimensional WAF is calculated by using Eq. (38) of Takaya and Nakamura (2001). The **W** vector is parallel to the Rossby group velocity and its divergence represents the divergence forcing of waves. In this study, it is calculated based on the perturbation stream function and time mean winds for boreal winter (November to March) at 200 hPa.

To elucidate the key process leading to the significant SAT anomaly during different MJO phases over the region of interest, the temperature tendency equation is analyzed. The intraseasonal perturbation thermodynamic equation can be expressed as:

$$\left\{\frac{\partial T}{\partial t}\right\}=\text{-}\left\{u\frac{\partial T}{\partial x}\right\}-\left\{v\frac{\partial T}{\partial y}\right\}+\{\omega\sigma\}+\left\{\frac{\dot{Q}}{C_p}\right\} \tag{2.4}$$

where $\sigma=\left(\frac{RT}{C_p p}\right)-\left(\frac{\partial T}{\partial p}\right)$ is the static stability, R is the gas constant, c_p is the specific heat of air, $\dot{Q}$ denotes the atmospheric apparent heat source (Yanai et al., 1973). The rest symbols follow convention in meteorology.

In Eq. (2.4) each separate variable can be decomposed into mean and anomaly fields and the latter can be further divided into MJO and non-MJO components (Seo et al., 2016):

$$A=\overline{A}+A^{'}\text{ and }A^{'}=\{A\}+A^{*} \tag{2.5}$$

where the overbar denotes the wintertime (December to March) mean and the prime is the total anomaly. Curly brackets and asterisk indicate the MJO and non-MJO components, respectively. The MJO component was obtained using a band-pass filter and the non-MJO component was denoted as the difference between the total anomaly and the MJO component. For example, the zonal advection term can be expressed as:

$$-\left\{u\frac{\partial T}{\partial x}\right\}=-\left\{(\overline{u}+\{u\}+u^{*})\frac{\partial(\overline{T}+\{T\}+T^{*})}{\partial x}\right\}=-\left\{\overline{u}\frac{\partial\overline{T}}{\partial x}\right\}-\left\{\overline{u}\frac{\partial\{T\}}{\partial x}\right\}-\left\{\overline{u}\frac{\partial T^{*}}{\partial x}\right\}-\left\{\{u\}\frac{\partial\overline{T}}{\partial x}\right\}-\left\{\{u\}\frac{\partial\{T\}}{\partial x}\right\}-\left\{\{u\}\frac{\partial T^{*}}{\partial x}\right\}-\left\{u^{*}\frac{\partial\overline{T}}{\partial x}\right\}-\left\{u^{*}\frac{\partial\{T\}}{\partial x}\right\}-\left\{u^{*}\frac{\partial T^{*}}{\partial x}\right\} \tag{2.6}$$

An anomalous GCM (AGCM) (Li, 2006) is used to analyze the extratropical response to specific MJO-related tropical forcing during boreal winter. This model was constructed on the basis of the dry version of the Princeton AGCM developed by (Held and Suarez, 1994). The global spectral model uses sigma (σ=p/p_s) as its vertical coordinate and there are five evenly distributed sigma levels with an interval of 0.2. The horizontal resolution is T42. The model is linearized by a specific 3D basic state (e.g., the winter mean basic state) derived from the long time mean of the NCEP-NCAR reanalysis to investigate the response of the atmosphere to a specific heating anomaly based on a realistic mean state. In this study, the model is forced with an anomaly heating resembling the observed OLR pattern over the Indian Ocean and the heating has an idealized vertical profile with the maximum heating rate at σ = 0.3 (about 300 mb). This vertical profile is consistent with that used to examine the direct response of global atmospheric circulation anomalies to MJO convection in the numerical study of Seo and Sun (2012) and Hu et al. (2019).The anomaly atmospheric GCM has been employed in the study of the mechanism responsible for the boreal summer MJO reinitiation in the equatorial Indian Ocean (Jiang and Li, 2005), the origin of wave train on synoptic scale in the western North Pacific (Li, 2006) and the wave train triggered by the tropical heating anomaly related to the convection of summer MJO in the northern hemisphere (Diao et al., 2018). A detailed introduction of this model was given in the appendix of Li (2006).

3. Results

3.1. Connections between the MJO and high-latitude SAT anomaly

In order to investigate the variability of wintertime (November to March) SAT in Northern Hemisphere, shown in Fig. 1a is the standard deviation of wintertime daily mean SAT. The high-latitude (poleward of 60 °N) SAT appears to have relatively larger variability compared with that of tropics and mid-latitudes. Considering the profound SAT variability poleward of 60 °N, fast Fourier

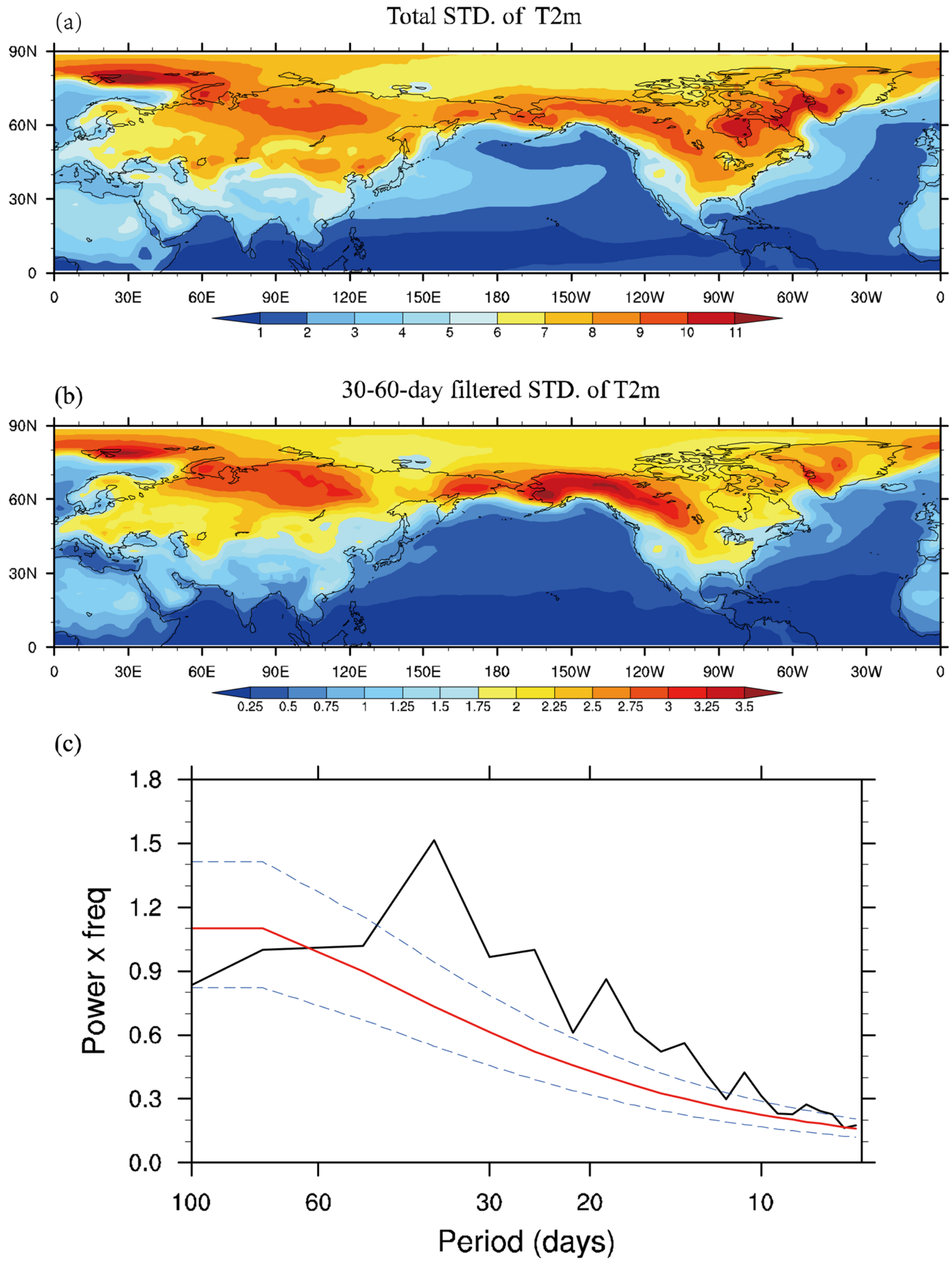

Fig. 1. Standard deviation of wintertime (November to March) (a) daily mean surface air temperature and (b) 30–60-day filtered surface air temperature anomalies in northern hemisphere during 1979–2016. (c) Power spectra of wintertime SAT over high latitudes (60°–90 °N, 180 °E–180 °W). Dash curve represents the 95 % significant level of red noise spectrum (red solid curve). (For interpretation of the references to colour in the Figure, the reader is referred to the web version of this article).

transform (FFT) is applied to the area-averaged daily SAT time series. The spectra are displayed in the area-conserving format where variance is proportional to area (Zangvil, 1977). The power spectrum of SAT variability in each year is firstly obtained after removing the annual cycle, and then the averaged result for the 38 years of 1979–2016 is used. The red noise spectrum is calculated according to Eq. (5) of Gilman et al. (1962) and the degree of freedom is 2*nsea (nsea is the number of seasons; 37 winters from 1979/80–2015/16). As shown in Fig. 1c, statistically significant spectrum peaks (relative to the red noise) can be found in the 10–60-day intraseasonal time scale in the spectral analysis. The ratio of the standard deviation of the 10–60-day intraseasonal time scale variability to that of the daily data is calculated (figure omitted) as well and the intraseasonal variability accounts for over 60 percent of the total SAT variability at high latitude in Northern Hemisphere. It can be found that the spectrum peak at 30–60-day time scale is more statistically significant. We also calculated the standard deviation of the 30–60-day filtered SAT (Fig. 1b) and found that the

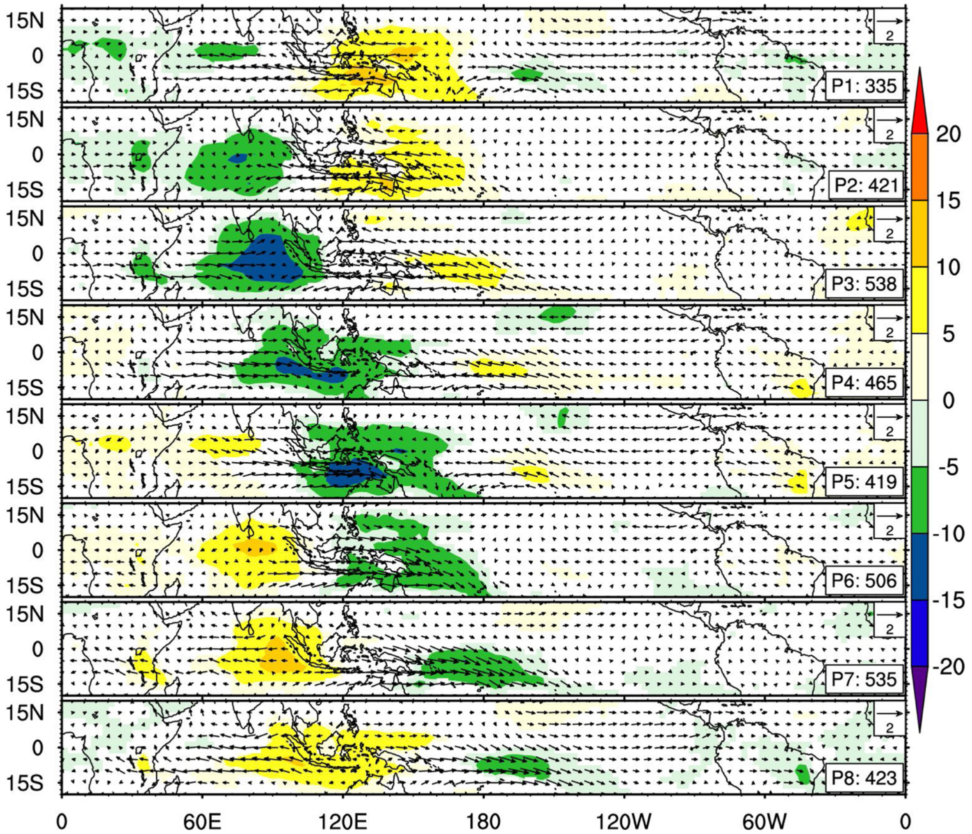

Fig. 2. Composite of 30–60-day filtered OLR (shading; W m^{-2}) and 850-hPa wind (vector; m s^{-2}) anomalies for each active MJO phase during wintertime. Shading are the areas exceeding the 95 % confidence level (Student t-test). The number of days of each phase is marked at the bottom right in each map.

SAT anomalies still shows relatively large variability over polar region on such a typical MJO time scale.

The propagation of the MJO can be naturally divided into eight phases by using the RMM index, corresponding to the eastward propagation of the enhanced convection from the Indian Ocean to the Pacific. It should be noted that we only take the active MJO events into account, depending on whether the RMM amplitude ($\sqrt{\mathrm{RMM1}^2 + \mathrm{RMM2}^2}$) is greater than 1 or not.

To reveal the tropical anomalous circulation characteristics associated with the MJO convection, shown in Fig. 2 is the simultaneous composites of the anomalous OLR and 850-hPa wind fields during different MJO phases. During phase 1, enhanced convective activity is located over Africa and western Indian Ocean, while suppressed convection is present in the central Pacific. At the same time, westerly wind anomalies exist over the Pacific, while easterly anomalies appear over the Indian Ocean. Then the eastward propagation of the MJO convection can be found in the following phases, passing through the eastern Indian Ocean, Maritime Continent and Pacific subsequently. To investigate whether the high latitude intraseasonal SAT variability is related to the MJO convection, we regressed the OLR anomalies onto the time series of the 30–60-day filtered SAT anomalies averaged over the entire polar cap (Fig. 3). Suppressed convection can be found over the Maritime Continent along the equator while enhanced convection is present over the western Pacific, Africa and western hemisphere. This indicates that the intraseasonal SAT signals over high latitude may be linked to the low frequency MJO activity.

Fig. 4 further confirms the modulation of SAT anomaly by the MJO convection. (Jin and Hoskins, 1995) proved that the direct global Rossby wave responding to the fixed tropical heating is established in about 15 days. Hence, in this study lagged composites of SAT anomalies for MJO phases with lag days 0, 4, 9, 13 are shown in the analysis below.

As has been demonstrated in many previous studies, phases 1–4 and phases 5–8 represent two opposite halves of the MJO life cycle. The lagged composite maps of SAT anomalies during these two half cycles show similar characteristics of symmetry. For brevity, we will focus on the subarea (180°–60°W, 60 °–90°N) with significant SAT anomalies during the MJO phase 3 and phase 7 throughout this study. A significantly negative SAT anomaly over the region of interest appears a few days later following the MJO phase 3 (Fig. 5). Conversely, the same region over high latitude is covered by a significantly positive SAT anomaly after the convective activity of the MJO appears in phase 7. Note that the amplitude of the positive and negative SAT anomalies are not symmetric between the two phases. The magnitude of SAT in phase 7 is significantly larger than that in phase 3, suggesting that the extratropical response is nonlinear to the MJO heating, which may account for the intraseasonal peaks in the entire norther polar cap region in Fig. 1 (c). Lastly, the connection between the MJO convective activity and high-latitude SAT anomaly may be not only limited to

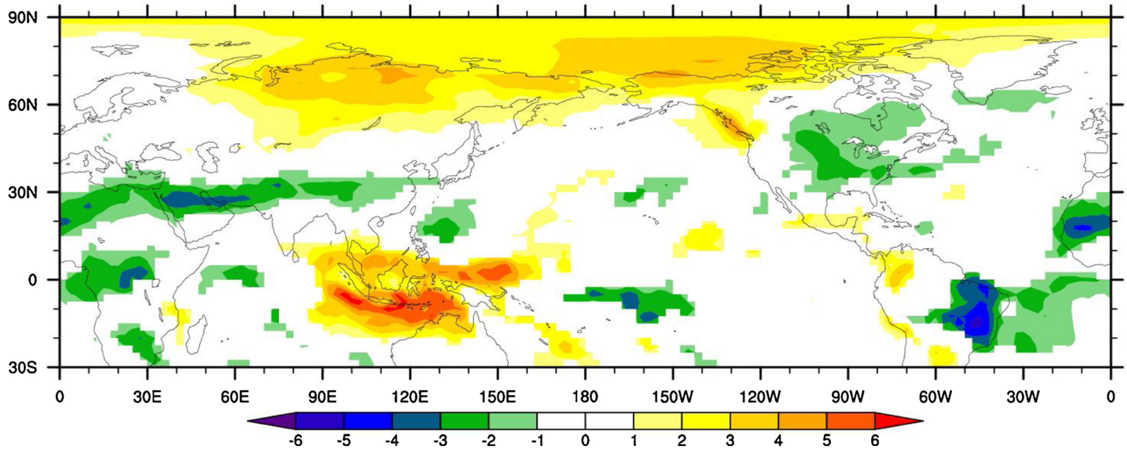

Fig. 3. Regression of the OLR anomalies onto the time series of the 30–60-day filtered SAT anomalies averaged over 60–90 N. Only the fields exceeding the 95 % confidence level based on a Student's *t*-test and its effective degree of freedom are shown.

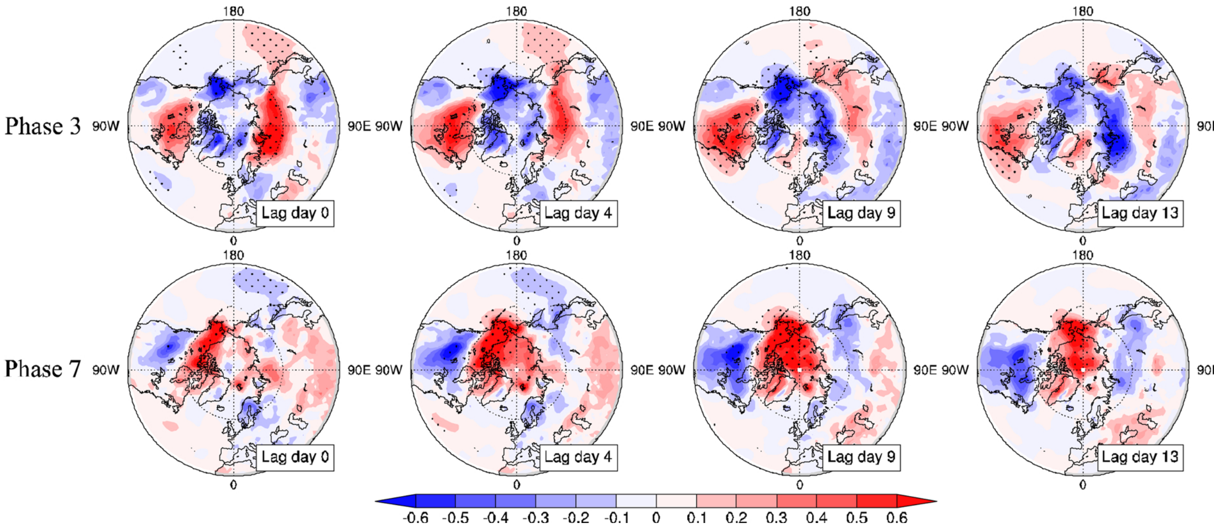

Fig. 4. Lagged composite of SAT anomaly (K) for MJO phase 3 (upper panel) and 7 (bottom panel). Lag days 0, 4, 9 and 13 are shown. Black dots represent values exceeding the 95 % confidence level (Student t-test).

phase 3 and phase 7. It can be found in other MJO phases as well. We conducted the composites of the SAT anomaly during phases 1, 2, 4 (5, 6, 8) with the same lag days and found similar amplitude cooling (warming) (figure omitted).

Not only the SAT signals but also the whole troposphere temperature anomalies show similar relationships associated with different MJO phases. Fig. 5 shows the meridional-vertical cross sections of composite temperature anomaly (T') and geopotential height anomaly (Z') averaged along the longitude of 180 °−60°W. As shown, in MJO phase 3 (phase 7), negative (positive) temperature anomaly appears through the troposphere with its minimum (maximum) located at the low-level troposphere, accompanied with significantly negative (positive) geopotential height anomaly. Thus, the distribution characteristics of the whole troposphere temperature are consistent with that of the SAT for each MJO phase. Additionally, this equivalent barotropical structure for the temperature anomalies exist over the Siberia (60–150 °E) sector as well, where intraseasonal SAT anomaly can be found during MJO phases (Fig. 4), but with less significant signals.

3.2. Large-scale circulation anomalies

In order to investigate the connection between the high-latitude intraseasonal SAT signals and the MJO convection as observed above, in this section the extratropical response to the MJO-related tropical convection in is examined. Many studies have demonstrated that the circulation anomalies triggered by the MJO-related anomalous tropical heating can extend into extratropics by inducing a Rossby wave train (Ferranti et al., 1990; Hendon and Salby, 1996; Black, 1997; Matthews et al., 2004). Mechanisms of this teleconnection have been examined based on a detailed vorticity budget analysis (Mori and Watanabe, 2008) and an idealized simulation with linearized primitive equations (Seo and Lee, 2017).

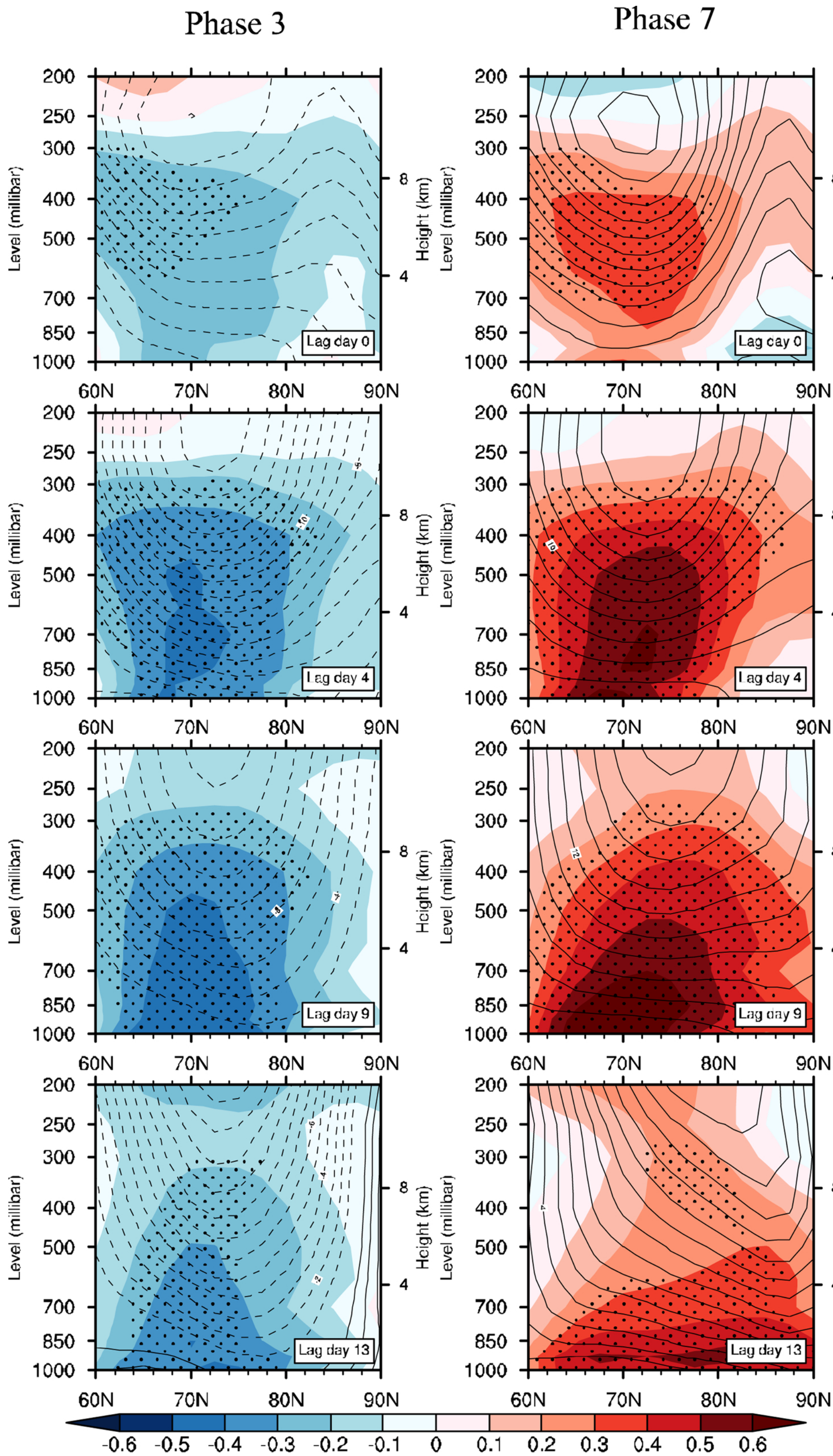

Fig. 5. The meridional-vertical distribution of lagged composite 30–60-day filtered temperature T′ (shading; K) averaged along the longitudes 180 °-60°W for MJO phase 3 (left) and phase 7 (right) during boreal winter. Lag days 0, 4, 9 and 13 are shown. Black dots represent values exceeding the 95 % confidence level (Student t-test).

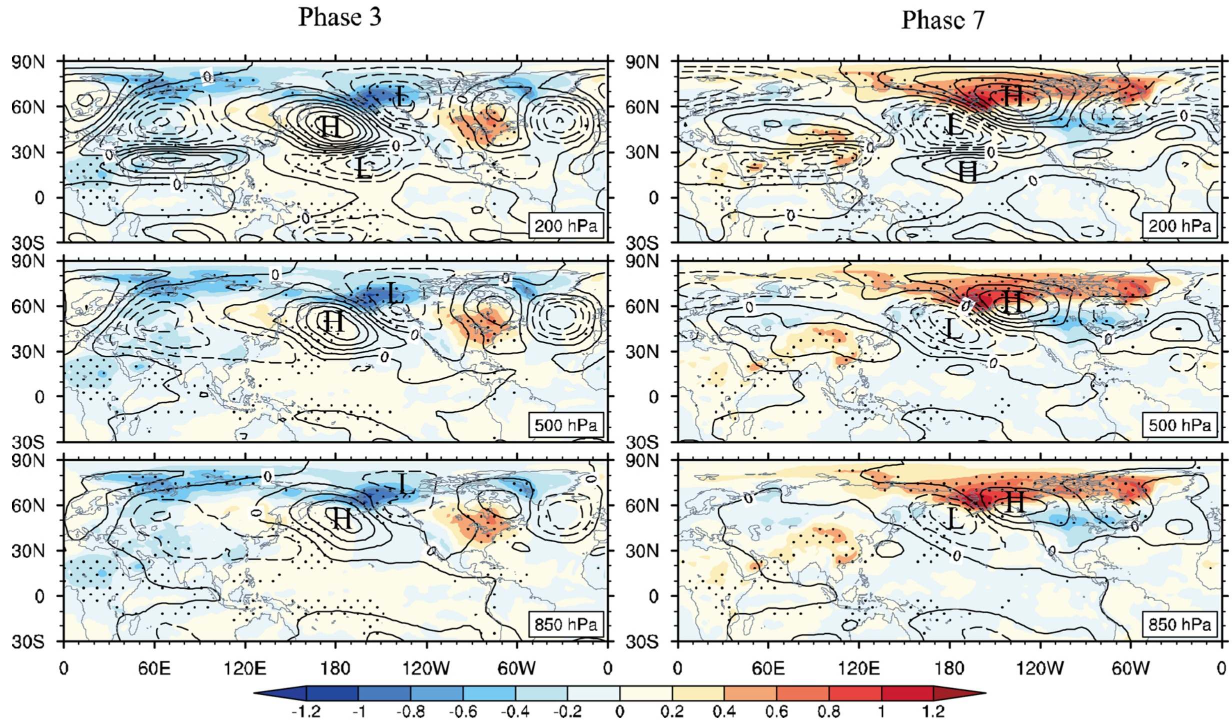

Fig. 6. Composite geopotential height anomaly fields (contour; with an interval of 4 gpm) at 200, 500, 850-hPa and SAT anomaly (shading; K) with a 3–11-day lag for MJO phase 3 (left) and phase 7 (right) during boreal winter. Black dots represent values exceeding the 95 % confidence level (Student t-test).

Fig. 6 depicts the composite of 200-hPa, 500-hPa and 850-hPa anomalous geopotential height during MJO phase 3 and 7 with a 3–11-day lag. (Branstator, 2014) has examined the midlatitude response to tropical heating that lasts 2 days and found that substantial signals can be detected even after 3 days. On average the effect of the local equatorial heating persists for at least two weeks. Therefore, a 3–11-day lagged composite analysis is adopted. We conducted same composites with different lag time as well and found similar results. For MJO phase 3, on the 3–11-day lagged composite map, global response to the MJO-related anomalous tropical forcing can be clearly seen from the 200-hPa anomalous circulation fields (upper panel of Figs. 6 and 7). The characteristics of the anomalous circulation fields in tropics can be regarded as an equatorial Rossby-Kelvin wave in response to the tropical forcing as shown in Fig. 2 (Gill, 1980). Extratropical circulation anomalies show corresponding response to it as well. A significant positive height anomaly centered at 45 ° N, 180 ° appears over the North Pacific, corresponding to an anticyclonic anomaly in 200-hPa wind anomalies field due to the quasi-geostrophic relation. A significantly negative height or cyclonic anomalies can also be found over the region we have focused on (180°–60°W, 60 °–90°N). The anomalous circulation patterns over high latitude are quite similar throughout the troposphere, and their amplitude decreases towards the surface, leading to the contraction of the air column between two constant pressure levels. There will be a colder temperature between them according to the hydrostatic relation. This may account for the negative SAT anomaly in the region of interest for phase 3. An opposite wave train pattern in the circulation anomalies fields appears during phase 7, as the tropical heating anomaly shows an opposite sign.

To identify the Rossby wave source that triggers the extratropical teleconnection patterns, we use the perturbation RWS defined as $S' \approx -\bar{\zeta}\nabla\cdot v'_x - v'_x\cdot\nabla\bar{\zeta}$. Fig. 9 reveals that strong RWS (shading) occurs along the East Asia jet (25 °–40°N, 110°E –180 °), corresponding to the positive anomalous heating over the Indian Ocean and negative heating anomaly over the western Pacific during MJO phase 3 (Fig. 2). The MJO phase 7 can generate an identical RWS pattern with opposite signs near the jet region. The jet regions are characterized by the large zonal and meridional wind gradients and the divergent flow is greater at the edge of the heating region, thus providing favorable conditions for a strong Rossby wave source. The wave activity flux **W** is overlaid on Fig. 8 as thick, black vectors. Pronounced northeastward propagating **W** vectors can be found located to the northeast of the strong RWS region over the subtropical Pacific, forming a wave train over North Pacific and North America. This indicates that the observed wave train pattern is likely due to the energy dispersion of the Rossby wave source, which generally originates from MJO convections over the Indian Ocean and western Pacific.

3.3. Cause of the extratropical circulation anomalies in MJO: Anomaly GCM experiments

To access the effect of the MJO-related anomalous tropical heating on organizing extratropical circulation anomaly, we conducted anomalous atmospheric GCM experiments with a positive specific heating centered on the equator at around 90 °E in the Indian

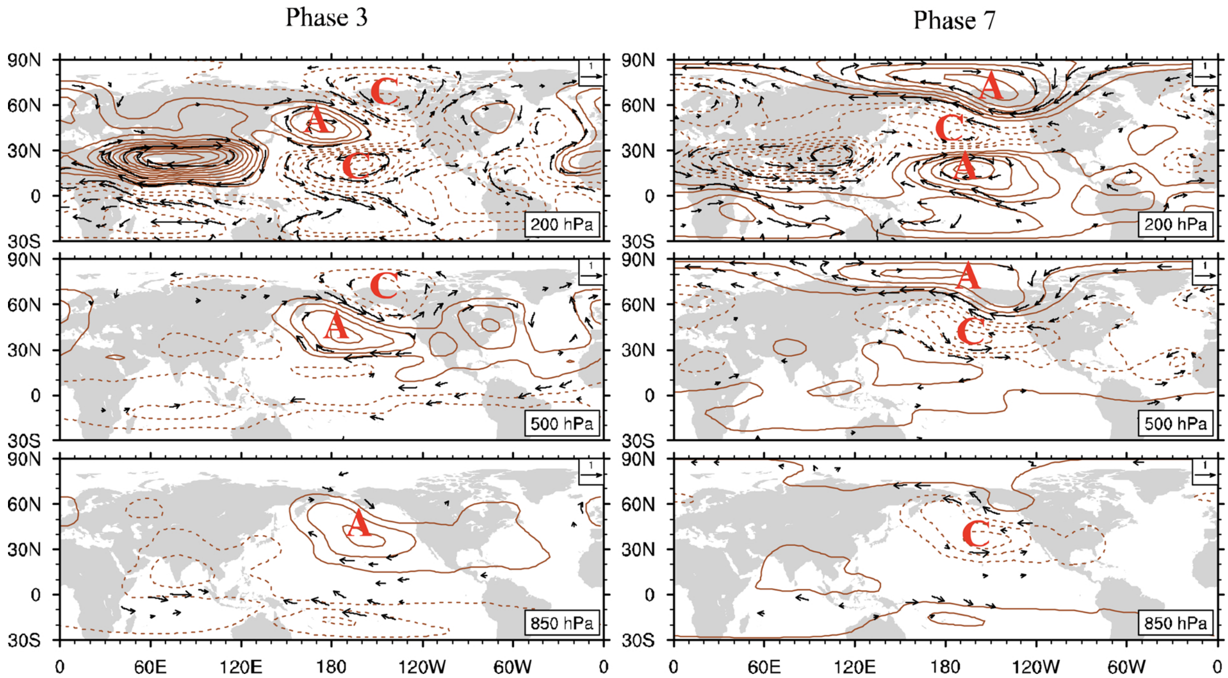

Fig. 7. Composite anomalous streamfunction (contours; $5 \times 10^5\,m^2\,s^{-1}$ interval) and wind (vector; $m\,s^{-1}$; only values exceeding $0.4\,m\,s^{-1}$ are shown)anomaly fields at 200, 500, and 850-hPa with a 3–11-day lag for MJO phase 3 and phase 7 during boreal winter.

Ocean. The location of the heating (Fig. 9a) corresponds to enhanced MJO convection during phase 3 (Fig. 2). Shown in Fig. 9b is the simulated 200-hPa geopotential height anomaly field. The average result of the last 30 days in the model is used to represent the steady-state response to the heating. Overlaid as shading is the observed circulation anomaly 3–11-days following the MJO phase 3 as depicted in Fig. 7. As illustrated in the simulated result, a dominant feature is that a wave train pattern exists over the North Pacific and it resembles the observed one during the MJO phase 3. The location of the simulated wave train has a little shifting compared with the realistic results. It is probably due to the model systematic biases. As illustrated in the simulated result, an anomalous high-pressure center is found over the north-west and south-west flank of the forcing region, over the north-east of which an anomalous low-pressure center can also be found. The features of the extratropical circulation anomalies can be seen in the simulated map as well, where an anomalous high-pressure anomaly appears over North Pacific, together with a low-pressure anomaly to the south and a high-pressure center to the north. In a word, the numerical model result confirms the hypothesis that the wave train observed in extratropical region is attributed to the MJO-related anomalous heating at tropics.

3.4. A temperature budget analysis

In order to have a better understanding of the key process contributing to the significant intraseasonal SAT anomaly at high latitude in the key region (180°−60°W, 60 °−90°N), we diagnosed the temperature budget equation [Eq.(2.4)] near the surface (925 hPa) during different MJO phases. Firstly, we calculated the areal averaged (180°−60°W, 60 °−90°N) value of the surface air temperature anomaly T' and its change rate $\frac{\partial T'}{\partial t}$ at different lag days (Fig. 10). The strongest temperature change rate and temperature anomaly tend to appear at around day 0 and day 10, respectively, for MJO phase 3 and phase 7. We have conducted the same calculation to the near-surface (925 hPa) temperature anomaly and found similar results. Considering the significant intraseasonal SAT signal and the large-scale circulation anomaly with a 3–11-day lagged composite, we conducted an averaged analysis between day +3 and day +11 in the following diagnosis to make the results more robust. The diagnosis results show marginal difference compared with that of the day with the strongest SAT signals (around day +10). How individual budget term contributes to the areal-averaged anomalous temperature tendency is clearly illustrated in Fig. 11. Note that since the diabatic heating term was diagnosed from the temperature equation with the original daily reanalysis data according to Yanai et al. (1973), the temperature budget is exactly in balance. The diagnosis result indicates that both the zonal and meridional temperature advection associated with anomalous circulation of 30–60-day variability contribute to the near-surface temperature anomaly during MJO phase 3 and phase 7.

Fig. 12 and 13 are the diagnosis results when we decompose the zonal temperature advection $-\left\{u\frac{\partial T}{\partial x}\right\}$ and the meridional temperature advection $-\left\{v\frac{\partial T}{\partial y}\right\}$ into nine terms according to Eq. (2.6). It reveals that the contribution mainly arises from two terms, $-\left\{\{u\}\frac{\partial \bar{T}}{\partial x}\right\}$ (bar 4 in Figs. 12a and 13 a) and $-\left\{\{v\}\frac{\partial \bar{T}}{\partial y}\right\}$ (bar 4 in Fig. 12b and Fig. 13b). This indicates that the advection of the mean temperature by the anomalous wind associated with the anomalous circulation of 30–60-day time scale makes the major contribution

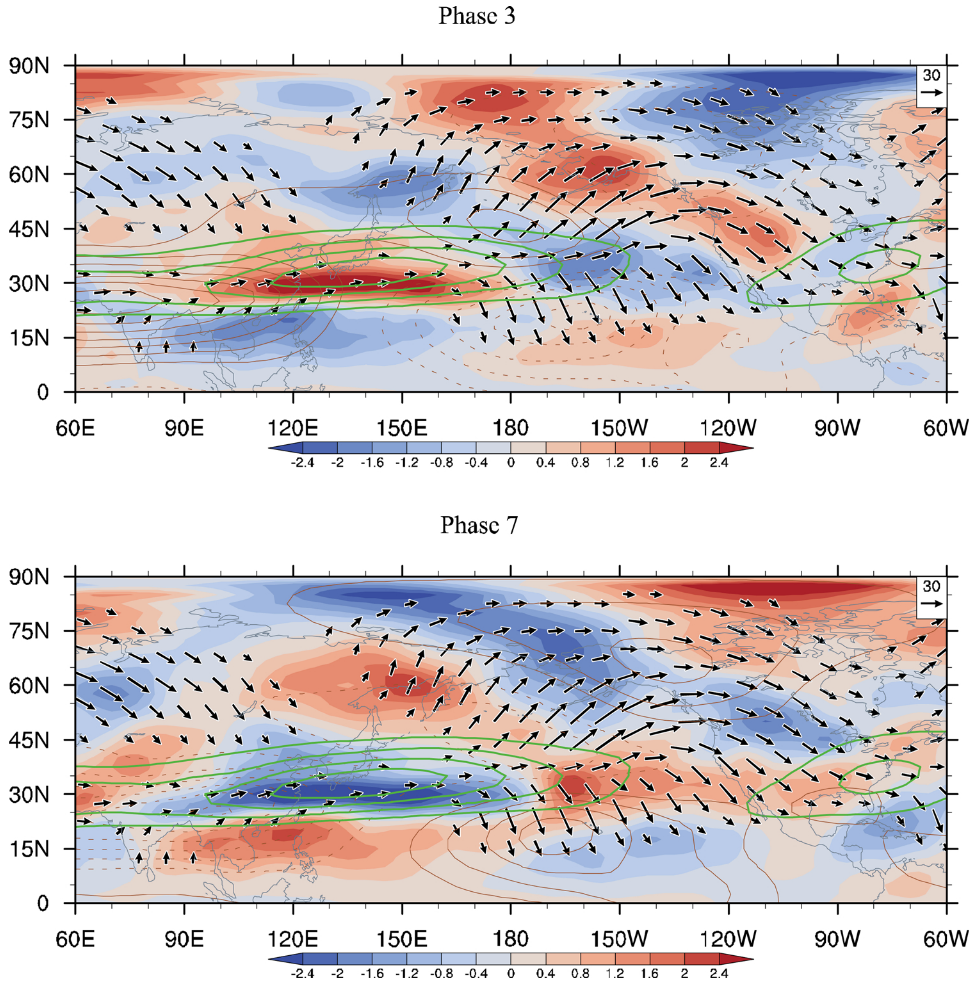

Fig. 8. Horizontal patterns of anomalous Rossby wave source (shading; 10^{-10} s^{-2}) and wave activity flux (vectors; m^2 s^{-2}; only values exceeding 15 m^2 s^{-2} are shown) during MJO phase 3 and phase 7 with a 3–11-days lag; 200-hPa streamfunction anomalies (red contours; 10^6 m^2 s^{-1} interval) and 200-hPa climatological zonal wind (green contours; 10 m s^{-1} interval; with only values exceeding 30 m s^{-1} shown). Contours with negative values are dashed. (For interpretation of the references to colour in the Figure, the reader is referred to the web version of this article).

to the temperature anomaly at the near surface. Compared with the advection of the mean temperature by the anomalous zonal wind, the advection of the mean temperature by the meridional wind anomaly plays a more significant role in the temperature anomaly over the high latitude, especially for the composite of MJO phase 3. The advection of the anomalous temperature by the mean wind flow (bar 2 in Figs. 12 and 13) and the advection of the mean temperature by the non-MJO wind flow (bar 7 in Figs. 12 and 13) also play a role in the anomalous temperature tendency, while the interaction between the non-MJO components (bar 9 in Figs. 12 and 13) primarily makes opposite contribution to the negative (positive) anomalous temperature tendency in phase 3 (phase 7). To have a clear understanding of how the dominant terms contribute to the anomalous temperature tendency, Fig. 14 and 15 illustrate the horizontal distributions of separate components of $-\left\{\{v\}\frac{\partial\bar{T}}{\partial y}\right\}$ and $-\left\{\{u\}\frac{\partial\bar{T}}{\partial x}\right\}$, respectively. For MJO phase 7, significant southerly anomalies and northerly anomalies are located to the west and east, respectively, of 120 °W (Fig. 14b). The wind anomaly is consistent with the large-scale anomalous circulation of 30–60-day time scale, corresponding to the anticyclonic anomaly over the key region for MJO phase 7. The stronger 30–60-day southerly anomaly transports the warm air towards higher latitude, resulting in the positive temperature anomaly at the near surface. The phase 3 shows similar horizontal distribution characteristics, except for a reversal of sign. Similarly, in Fig. 15b, significant easterly anomalies and westerly anomalies are found located to the south and north, respectively, of around 65 °N for MJO phase 7. The strong anomalous westerlies transport the warmer air eastward, resulting in the warm advection east of around 120 °W. In general, the advection of the mean temperature by the anomalous meridional and zonal wind associated with the anomalous circulation of MJO-related variability work together, making the major contribution to the significant temperature anomaly at the near surface and the SAT signals over the high latitude during boreal winter.

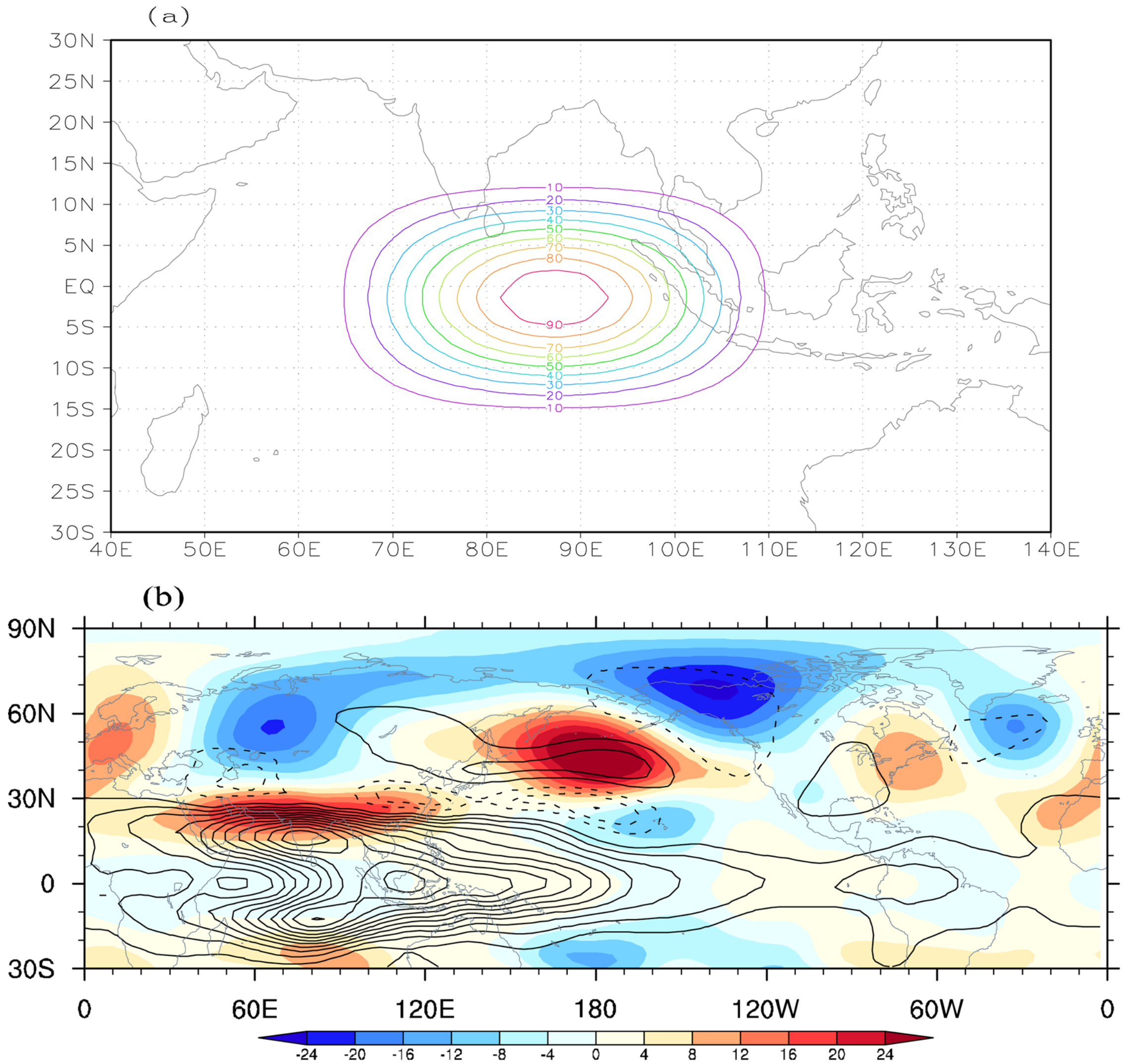

Fig. 9. (a) Horizontal distribution of the diabatic heating (10^{-2} K day^{-1}) prescribed in the AGCM. The pattern is derived from the negative OLR (convection) distribution over the Indian Ocean from phase 3 in Fig. 3. (b) Simulated geopotential height anomaly (gpm) field at 200-hPa (contour; with an interval of 5 gpm) from the AGCM in response to anomalous heating in the tropical Indian Ocean during MJO phase 3. Shading is the observed geopotential height anomaly fields (gpm) at 200 hPa from phase 3 in Fig. 6. The zero lines are omitted.

4. Conclusions

In the current study the impact of the MJO on high-latitude SAT during boreal winter is examined. Based on 38-yr (1979–2016) surface air temperature at 2 m (T2 m) from NCEP-NCAR re-analysis data and the bivariate MJO index proposed by (Wheeler and Hendon, 2004) in boreal winter (November to March), significant connections between the intraseasonal SAT signals over high latitude and the MJO-related tropical convection are found. Throughout the study, we mainly focus on two phases in two opposite halves of MJO life cycles, phase 3 and phase 7, corresponding to the enhanced convection of the MJO over the eastern Indian Ocean and western Pacific respectively. Considering that extratropical in response to tropical heating anomaly may lag a few days, usually one to two weeks, we conduct the SAT composites with different lag days to make the results more significant. A negative SAT anomaly over high latitude appears after MJO convection propagates into phase 3, while a positive one appears a few days following the MJO phase 7. The connection between the MJO and high-latitude SAT anomalies is relatively significant and consistent over the subarea 180 °–60°W, 60 °–90°N. The vertical structures of the temperature over the region show similar connections with MJO phases throughout the troposphere. An analysis of the 3–11-days lagged composites of anomalous circulation fields indicates that the tropical convective activity may have a remote impact on the high-latitude SAT anomaly, taking the form of a Rossby wave train. The wave train pattern observed over North Pacific during an MJO life cycle has been clearly illustrated in (Matthews et al., 2004). It is defined to be negative and positive according to the extratropical circulation anomalies patterns in the North Pacific. The location of the anomalous heating for these two North Pacific patterns described in their study is exactly corresponding to that of MJO phase 3

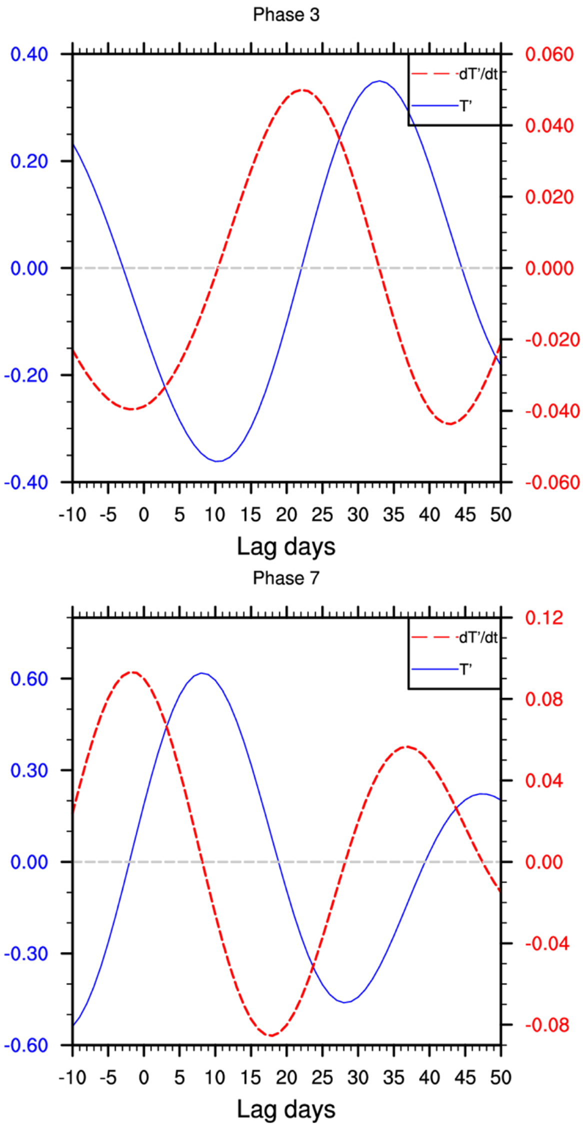

Fig. 10. Time evolution of surface air temperature anomaly (K) and its tendency (K day^{-1}) averaged in the box (180°–60 °W, 60 °N–90 °N) during lag –10 to lag +50 day for MJO phase 3 and phase 7 during boreal winter.

and phase 7, respectively. Analysis of the perturbation Rossby wave source and wave activity flux indicates that the observed wave train over the North Pacific is primarily a result of the northeastward propagating Rossby wave source triggered by MJO-related tropical forcing through Rossby wave energy dispersion. To better understand the role of the MJO-related anomalous tropical heating in organizing the extratropical circulation anomalies, numerical model experiment with the aid of an anomaly atmospheric GCM is conducted. The result of the experiment reveals that the specific tropical forcing related to the MJO phases can lead to the Rossby wave pattern in extratropics. Thus, the MJO can have a remote influence on the anomalous circulation and temperature over high latitude. The key process contributing to high-latitude intraseasonal SAT anomaly is further identified on the basis of a thermodynamic budget diagnosis at the near surface (925 hPa). Generally, the significant intraseasonal SAT signal over the high latitude during boreal winter is mainly attributed to the advection of the mean temperature by the wind anomaly associated with the anomalous circulation of MJO-related variability.

Considering the fact that the MJO represents a primary source of predictability on the intraseasonal time scale and great improvement has been achieved in dynamic MJO prediction during the last decades, the observed lagged relationship between the MJO phases and the SAT anomaly may be served as a helper for extended-range forecast of high-latitude SAT during boreal winter. However, it should be noted that the lagged composite maps discussed above only show an average result of numerous diverse MJO

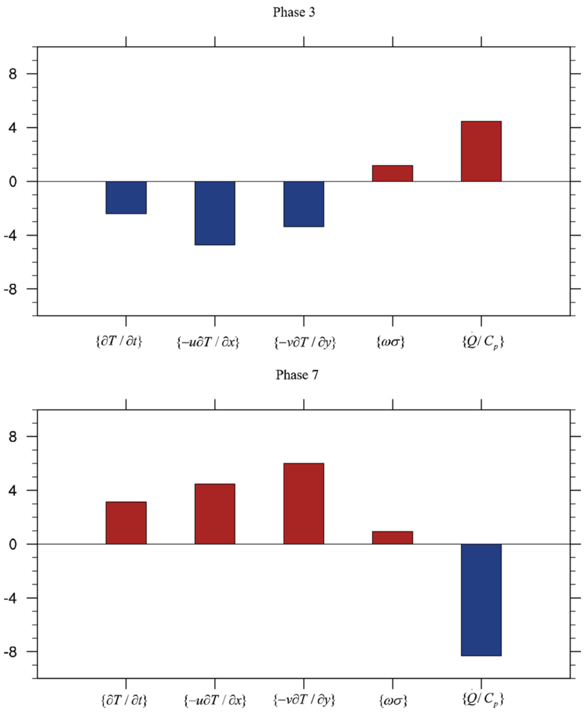

Fig. 11. Temperature budget averaged in the box (180°—60 °W, 60 °N—90 °N) at 925 hPa for day +3 to day +11 composite during MJO phase 3 (10^{-7} K s^{-1})and phase 7. Terms from left to right are temperature change, zonal advection of temperature, meridional advection of temperature, adiabatic heating and diabatic heating.

events and not all the MJO events have the same characteristics of propagation and amplitude. Additionally, high-latitude SAT is mostly affected by mid-latitude and high-latitude variabilities itself, so the MJO should only be considered as a supplementary contributor. Considering that we will further take the influences from mid-latitude variabilities such as the Arctic Oscillation and the interactions with transient eddies into account in the next work.

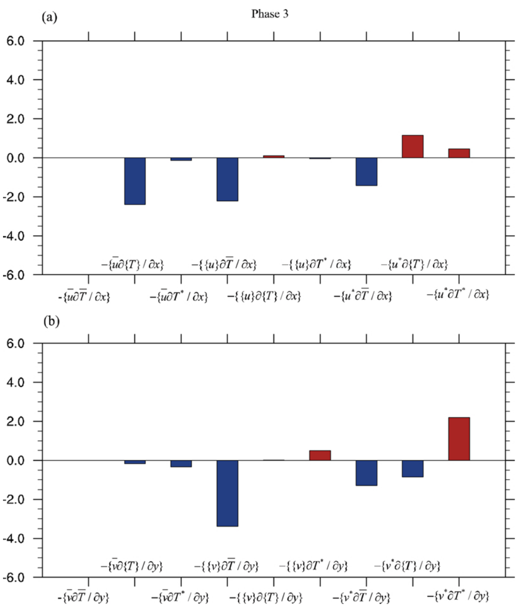

Fig. 12. Individual terms of $-\left\{u\frac{\partial T}{\partial x}\right\}$ (a) and $-\left\{v\frac{\partial T}{\partial y}\right\}$ (b) (10^{-7} K s^{-1}) averaged in the same box at 925 hPa for day +3 to day +11 composite for MJO phase 3 during boreal winter.

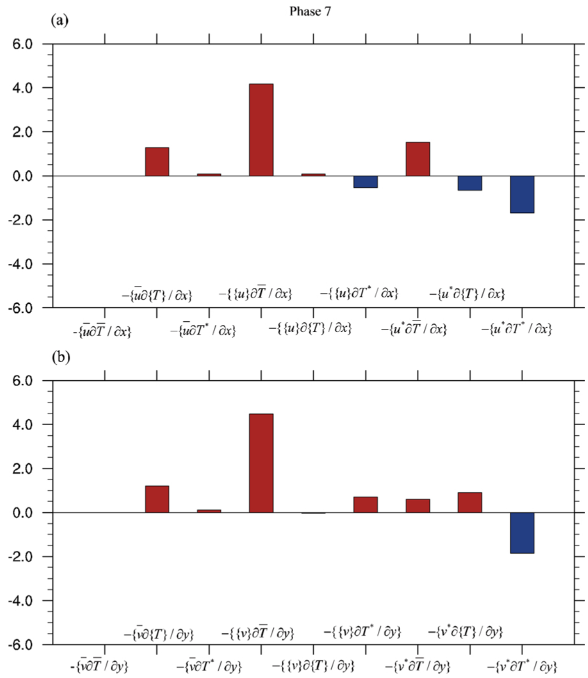

Fig. 13. As in Fig.13, but for the composites for MJO phase 7.

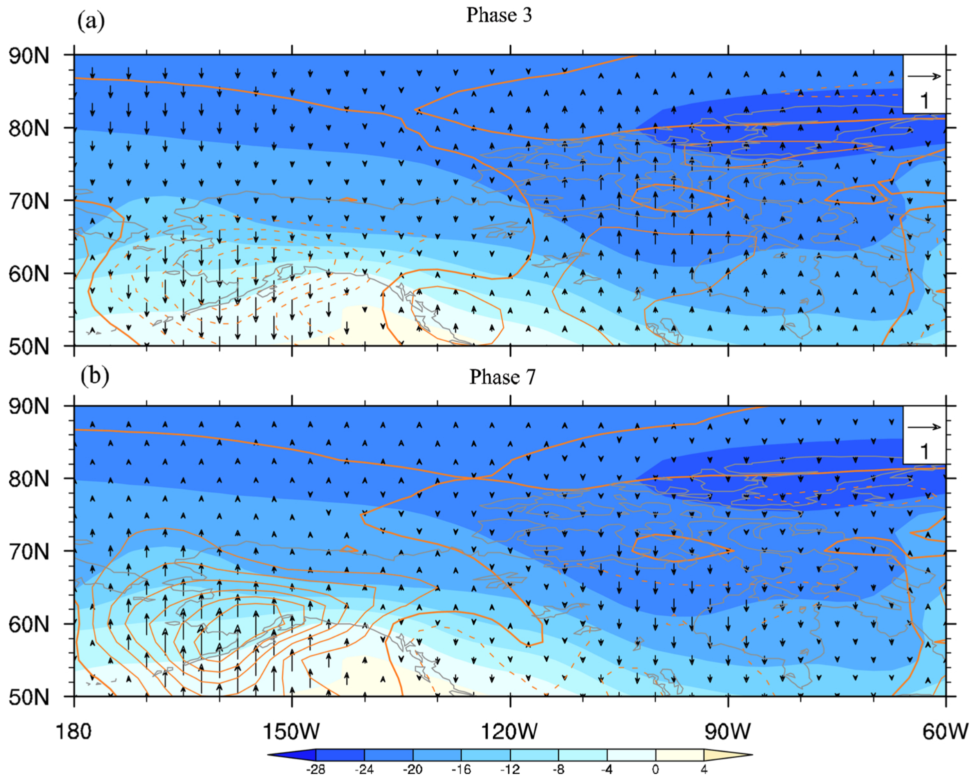

Fig. 14. A Horizontal distribution of the wintertime mean temperature $\overline{T}$ (shading; K), the anomalous meridional wind associated with MJO {v} (vector; m s^{-1}; see scale at the upper right corner), and $-\left\{\{v\}\frac{\partial\overline{T}}{\partial y}\right\}$ (contours; with an interval of 10^{-6} K s^{-1}; thick lines denote zero contours) at 925 hPa for day +3 to day +11 composite for MJO phase 3 (a) and phase 7 (b) during wintertime.

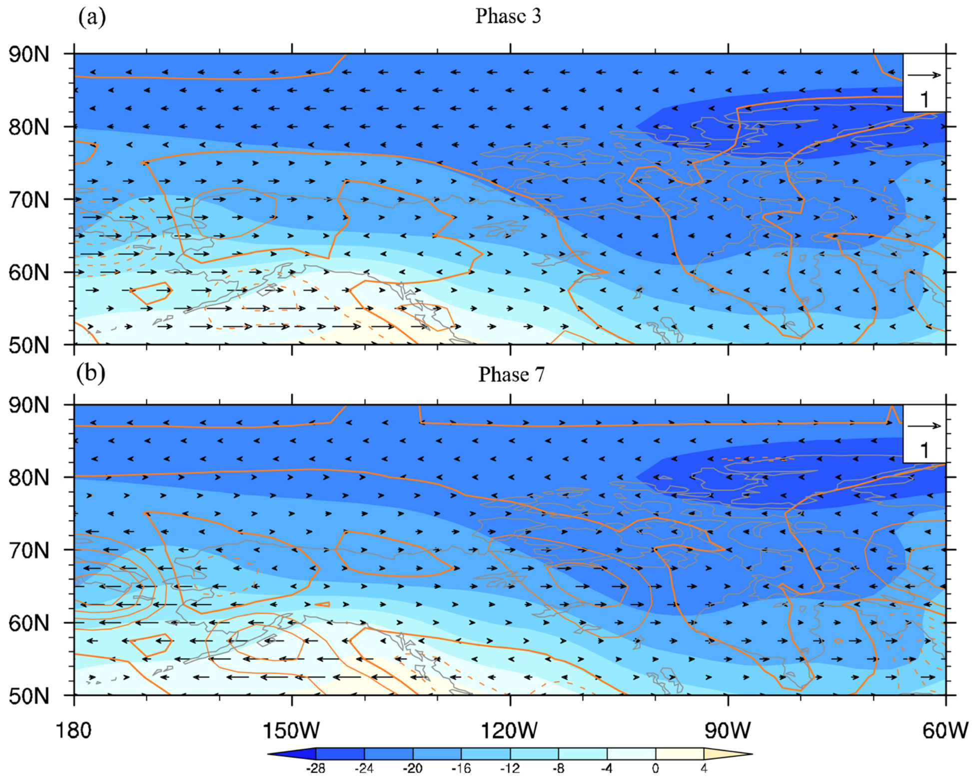

Fig. 15. A Horizontal distribution of the wintertime mean temperature $\overline{T}$ (shading; K), the anomalous zonal wind associated with MJO $\{u\}$ (vector; m s^{-1}; see scale at the upper right corner), and $-\left\{\{u\}\frac{\partial \overline{T}}{\partial x}\right\}$ (contours; with an interval of 5×10^{-7} K s^{-1}; thick lines denote zero contours) at 925 hPa for day +3 to day +11 composite for MJO phase 3 (a) and phase 7 (b) during wintertime.

CRediT authorship contribution statement

Jing Cui: Methodology, Software, Formal analysis, Visualization, Investigation, Data curation, Writing - original draft. **Shuangyan Yang:** Conceptualization, Methodology, Software, Validation, Formal analysis, Visualization, Investigation, Resources, Writing - review & editing, Supervision, Project administration, Funding acquisition. **Tim Li:** Conceptualization, Methodology, Formal analysis, Resources, Writing - review & editing.

Declaration of Competing Interest

The authors declare that they have no known competing financial interests or personal relationships that could have appeared to influence the work reported in this paper.

Acknowledgments

This work was supported by the National Key R&D Program of China (Grant No. 2018YFC1505905, 2018YFC1505602), the Natural Science Foundation of Jiangsu Higher Education Institutions of China (Grant No. 18KJB170015), the National Natural Science Foundation of China (Grant No. 41975048), and the Startup Foundation for Introducing Talent of NUIST (Grant No. 2018R027).The authors would like to thank the NOAA, NCEP-NCAR and Australian Bureau of Meteorology for the data and information provided.

Appendix A. Supplementary data

Supplementary material related to this article can be found, in the online version, at doi:https://doi.org/10.1016/j.dynatmoce.2020.101141.

References

Bergman, J.W., Hendon, H.H., Weickmann, K.M., 1999. Intraseasonal air–sea interactions at the onset of el niño. J. Climate 14, 1702–1719.

Black, R.X., 1997. Deducing anomalous wave source regions during the life cycles of persistent flow anomalies. J. Atmos. Sci. 54, 895–907.
Bond, N., Vecchi, G., 2003. The influence of the Madden–Julian oscillation on precipitation in Oregon and Washington. Weather. Forecast. 18, 600–613.
Branstator, G., 2014. Long-lived response of the midlatitude circulation and storm tracks to pulses of tropical heating. J. Clim. 27, 8809–8826.
Chang, C.P., Lim, H., 1988. Kelvin Wave-CISK: a possible mechanism for the 30-50 day oscillations. J. Atmos. Sci. 45, 1709–1720.
Diao, Y., Tim, L.I., Hsu, P.C., 2018. Influence of the boreal summer intraseasonal oscillation on extreme temperature events in the Northern Hemisphere. J. Meteorol. Res. 32, 20–33.
Ferranti, L., Palmer, T., Molteni, F., Klinker, E., 1990. Tropical-extratropical interaction associated with the 30–60 day oscillation and its impact on medium and extended range prediction. J. Atmos. Sci. 47, 2177–2199.
Gill, A.E., 1980. Some simple solutions for heat-induced tropical motion. Q. J. R. Meteorol. Soc. 106, 447–462.
Gilman, D.L., Fuglister, F.J., Mitchell, J.M., 1962. On the power Spectrum of "Red noise". J. Atmos. Sci. 20, 182–184.
Hall, J.D., Matthews, A.J., Karoly, D.J., 2001. The modulation of tropical cyclone activity in the australian region by the Madden–Julian oscillation. Mon. Wea. Rev. 129, 2970–2982.
Held, I., Suarez, M.A.X., 1994. A proposal for the intercomparison of the dynamical cores of atmospheric general circulation models. Bull. Am. Meteorol. Soc. 75, 1825–1830.
Hendon, H., Salby, M., 1996. Planetary-scale circulations forced by intraseasonal variations of observed convection. J. Atmo. Sci. 53, 1751–1760.
Higgins, R.W., Mo, K.C., 1997. Persistent north pacific circulation anomalies and the tropical intraseasonal oscillation. J. Clim. 10, 223–244.
Hong, C.C., Li, T., 2009. The extreme cold anomaly over Southeast Asia in February 2008: roles of ISO and ENSO. J Clim 22, 3786–3801.
Hsu, P.C., Li, T., 2012. Role of the boundary layer moisture asymmetry in causing the eastward propagation of the madden-julian oscillation. J. Clim. 25, 4914–4931.
Hu, W.T., Liu, P., Zhang, Q., He, B., 2019. Dominant patterns of winter-time intraseasonal surface air temperature over the CONUS in response to MJO convections. Clim. Dyn. 53, 3917–3936.
Jia, X., Chen, L., Ren, F., Chongyin, L.I., 2011. Impacts of the MJO on winter rainfall and circulation in China. Adv. Atmos. Sci. 28, 521–533.
Jiang, X.A., Li, T., 2005. Reinitiation of the boreal summer intraseasonal oscillation in the Tropical Indian Ocean. J. Clim. 18, 3777–3795.
Jin, F., Hoskins, B., 1995. The direct response to tropical heating in a baroclinic atmosphere. J. Atmos. Sci. 52, 307–319.
Kiladis, G., Weickmann, K.M., 1992. Circulation anomalies associated with tropical convection during northern winter. Mon. Weat Rev. 120, 1900–1923.
Kiladis, G.N., Dias, J., Straub, K.H., Wheeler, M.C., Tulich, S.N., Kikuchi, K., Weickmann, K.M., Ventrice, M.J., 2014. A comparison of OLR and circulation-based indices for tracking the MJO. Mon. Wea. Rev. 142, 1697–1715.
L'Heureux, M., Higgins, R., 2008. Boreal winter links between the Madden Julian Oscillation and the arctic oscillation. J. Clim. 21, 3040–3050.
Lau, K.M., Philips, T.J., 1986. Coherent fluctuations of extratropical geopotential height and tropical convection in intraseasonal time scales. J. Atmo. Sci. 43, 7810–7821.
Li, T., 2006. Origin of the summertime synoptic-scale wave train in the Western North Pacific. J. Atmos. Sci. 63, 1093–1102.
Li, T., 2014. Recent advance in understanding the dynamics of the madden-julian oscillation. J. Meteorol. Res. 28, 1–33.
Lin, H., Brunet, G., 2009. The influence of the madden-julian oscillation on canadian wintertime surface air temperature. Mon. Wea. Rev. 137, 2250–2262.
Lorenz, D.J., Hartmann, D.L., 2006. The effect of the MJO on the north american monsoon. J. Clim. 19, 333–343.
Madden, R.A., Julian, P.R., 1971. Detection of a 40-50 day oscillation in the zonal wind in the Tropical Pacific. J. Atmos. Sci. 28, 702–708.
Madden, R.A., Julian, P.R., 1972. Description of global-scale circulation cells in the tropics with a 40-50 day period. J. Atmos. Sci. 29, 1109–1123.
Madden, R., Julian, P., 1994. Observations of the 40–50-Day tropical oscillation—a review. Mon. Wea. Rev. 122, 814–837.
Maloney, E.D., Hartmann, D.L., 2000. Modulation of eastern north pacific hurricanes by the madden-julian oscillation. J. Clim. 13, 1451–1460.
Mao, J., Sun, Z., Wu, G., 2010. 20–50-Day oscillation of summer Yangtze rainfall in response to intraseasonal variations in the subtropical high over the western North Pacific and South China Sea. Clim. Dyn. 34, 747–761.
Matsueda, S., Takaya, Y., 2015. The global influence of the Madden–Julian oscillation on extreme temperature events. J. Clim. 28, 4141–4151.
Matthews, A., Hoskins, B., Masutani, M., 2004. The global response to tropical heating in the MJO during northern winter. Q. J. R. Meteorol. Soc. 130, 1991–2011.
Mori, M., Watanabe, M., 2008. The growth and triggering mechanisms of the PNA: a MJO–PNA coherence. J. Meteorol. Soc. Jpn. 86, 213–236.
Pai, D.S., Bhate, J., Sreejith, O.P., Hatwar, H.R., 2011. Impact of MJO on the intraseasonal variation of summer monsoon rainfall over India. Clim. Dyn. 36, 41–55.
Rao, S., Yamagata, T., 2004. Abrupt termination of Indian Ocean Dipole events in response to intraseasonal disturbances. Geophy. Res. Let. 31.
Sardeshmukh, P.D., Hoskins, B.J., 1988. The generation of global rotational flow by steady idealized tropical divergence. J. Atmos. Sci. 45, 1228–1251.
Seo, K.H., Lee, H.J., 2017. Mechanisms for a PNA-like teleconnection pattern in response to the MJO. J. Atmos. Sci. 74, 1767–1781.
Seo, K.H., Son, S.W., 2012. The global atmospheric circulation response to tropical diabatic heating associated with the Madden—Julian Oscillation during northern winter. J. Atmos. Sci. 69, 79–96.
Seo, K.H., Lee, H.J., Frierson, D.M.W., 2016. Unraveling the teleconnection mechanisms that induce wintertime temperature anomalies over the Northern Hemisphere continents in response to the MJO. J. Atmos. Sci. 73, 3557–3571.
Sobel, A., Maloney, E., 2013. Moisture modes and the eastward propagation of the MJO. J. Atmos. Sci. 70, 187–192.
Takaya, K., Nakamura, H., 2001. A formulation of a phase-independent wave-activity flux for stationary and migratory quasigeostrophic eddies on a zonally varying basic flow. J. Atmos. Sci. 58, 608–627.
Takayabu, Y.N., Iguchi, T., Kachi, M., Shibata, A..Amp, Kanzawa, H., 1995. Abrupt termination of the 1997-98 El Nino in response to a Madden-Julian Oscillation. Nature 402, 279–282.
Ting, M., Sardeshmukh, P., 1993. Factors determining the extratropical response to equatorial diabatic heating anomalies. J. Atmos. Sci. 50, 907–918.
Tseng, K.C., Maloney, E., Barnes, E., 2019. The consistency of MJO teleconnection patterns: an explanation using linear rossby wave theory. J. Clim. 32, 531–548.
Vecchi, Bond, N.A., 2004. The Madden-Julian Oscillation (MJO) and northern high latitude wintertime surface air temperatures. Geophy. Res. Let. 31, L04104.
Wang, B., Rui, H., 1990. Dynamics of the coupled moist kelvin–Rossby wave on an equatorial β -Plane. J. Atmos. Sci. 47, 397–413.
Wang, S., Sobel, A.H., Tippett, M.K., Vitart, F., 2019. Prediction and predictability of tropical intraseasonal convection: seasonal dependence and the Maritime Continent prediction barrier. Clim. Dyn. 52, 6015–6031.
Wen, M., Yang, S., Higgins, W., Zhang, R., 2011. Characteristics of the dominant modes of atmospheric quasi-biweekly oscillation over Tropical-Subtropical Americas. J. Clim. 24, 3956–3970.
Wheeler, M.C., Hendon, H.H., 2004. An all-season real-time multivariate MJO index: development of an index for monitoring and prediction. Mon. Wea. Rev. 132, 1917–1932.
Wilks, D.S., 2011. Statistical Methods in the Atmospheric Science, 3rd ed. Academic Press, pp. 676.
Yanai, M., Esbensen, S., Chu, J.-H., 1973. Determination of bulk properties of tropical cloud clusters from large-scale heat and moisture budgets. J. Atmos. Sci. 30, 611–627.
Yang, S., Li, T., 2016a. Intraseasonal variability of air temperature over the mid-high latitude Eurasia in boreal winter. Clim. Dyns. 47, 1–21.
Yang, S., Li, T., 2016b. Zonal shift of the south asian high on subseasonal timescale and its relation to the summer rainfall anomaly in China: zonal shift of the SAH on subseasonal timescale. Q. J. R. Meteorol. Soc. 142, 2324–2335.
Yang, S., Li, T., 2017a. Causes of intraseasonal diabatic heating variability over and near the Tibetan Plateau in boreal summer. Clim. Dyn. 49, 2385–2406.
Yang, S., Li, T., 2017b. The role of intraseasonal variability at mid-high latitudes in regulating Pacific blockings during boreal winter. Int. J. Climatol. 37 (Suppl.1), 1248–1256.
Yang, S., Zhu, Z., Cui, J., Yang, Y., 2019. Regulation of the intraseasonal oscillation over mid-to-high latitude Eurasia on winter surface air temperature over China. Dyn. Atmos. Oceans 86, 63–72.
Yoo, C., Lee, S., Feldstein, S.B., 2012. Mechanisms of arctic surface air temperature change in response to the madden-julian oscillation. J. Clim. 25, 5777–5790.
Zangvil, A., 1977. On the presentation and interpretation of spectra of large-scale disturbances. Mon. Wea. Rev. 105, 1469–1472.
Zhao, C., Li, T., Zhou, T., 2013. Precursor signals and processes associated with MJO initiation over the tropical Indian Ocean. J. Clim. 26, 291–307.
Zhou, S., Miller, A.J., 2003. The interaction of the madden-julian oscillation and the arctic oscillation. J. Clim. 18, 143–159.